Chemical Science

ROYAL SOCIETY OF CHEMISTRY

EDGE ARTICLE

View Article Online
View Journal | View Issue

Cite this: *Chem. Sci.*, 2026, **17**, 2791

All publication charges for this article have been paid for by the Royal Society of Chemistry

A unimolecular near-infrared fluorescent probe for *in vivo* imaging of enzymes with minimized false-negative signals

Jinliang Han,[a] Mingwang Yang,*[a] Chengyuan Lv,[a] Kang Li,[a] Jiangli Fan *[ab] and Xiaojun Peng [a]

Accurate imaging of specific enzymes is critical for the early diagnosis of ovarian cancer; however, conventional imaging agents often produce false-negative signals due to the heterogeneous expression of individual biomarkers, leading to delayed treatment and increased risk of disease progression. To address this limitation, we present **Cy-GGT–β-gal**, a unimolecular near-infrared (NIR) fluorescent probe engineered for the simultaneous detection of two key ovarian cancer biomarkers: γ-glutamyl transpeptidase (GGT) and β-galactosidase (β-gal). This dual-enzyme-responsive probe is designed to activate NIR fluorescence upon interaction with either GGT or β-gal through an intramolecular elimination mechanism, thereby significantly minimizing the likelihood of false-negative results. Compared to single-enzyme-targeting probes, **Cy-GGT–β-gal** demonstrates superior diagnostic reliability, enabling high-contrast discrimination (signal-to-noise ratio, SNR > 6.1) between multiple ovarian cancer cell lines (SHIN3, OVCAR3, OVCAR5, A2780, SKOV3) and normal cells. Furthermore, the probe successfully visualizes tumor lung metastases and nodular tissues with high specificity (SNR ∼ 11.2), underscoring its potential for precise *in vivo* imaging. This study not only introduces a robust unimolecular NIR fluorescent probe to mitigate false-negative diagnoses in ovarian cancer but also establishes a versatile design strategy for developing multi-enzyme-responsive imaging agents, offering a promising approach to enhance diagnostic accuracy in clinical settings.

Received 23rd September 2025
Accepted 16th November 2025

DOI: 10.1039/d5sc07381b

rsc.li/chemical-science

Introduction

Ovarian cancer ranks among the three most lethal malignancies of the female reproductive system.[1–4] Due to the anatomically concealed location of the ovaries and the absence of specific early symptoms, most patients are diagnosed at an advanced stage, which significantly compromises treatment efficacy and survival outcomes.[5–7] Therefore, early and accurate detection is critical for improving therapeutic success rates and long-term patient survival.[5,8–10] Among emerging diagnostic strategies, fluorescence imaging has emerged as a noninvasive, real-time, and high-resolution modality for ovarian cancer visualization.[11–17] Among various fluorochromes, hemicyanine dyes represent ideal candidates for phototheranostic applications due to their excellent properties, including NIR absorption/emission profiles ($\lambda_{max} \geq 680$ nm), large molar extinction coefficients, and modifiable photochemical sites that enable deep tissue penetration.[18–22]

The high catalytic efficiency and specificity of γ-glutamyl transpeptidase (GGT) and β-galactosidase (β-gal) have established these enzymes as key biomarkers for ovarian cancer, thereby facilitating their integration into activatable fluorescent probes.[7,13,23–28] In some cases, non-specific fluorescence may occur during enzyme detection, leading to the generation of false-positive signals.[29–32] Although dual-lock-activatable fluorescent probes that only emit fluorescence signals upon interaction with two biomarkers have been developed to mitigate this phenomenon, they may fail to detect lesions expressing a single biomarker, thereby reducing detection sensitivity.[33–36] More importantly, the heterogeneous and variable expression levels of GGT and β-gal across ovarian cancer subtypes pose another significant diagnostic challenge-"false-negative". Specifically, while GGT is overexpressed in OVCAR5 cells, it exhibits low expression in OVCAR3 cells, whereas β-gal displays the inverse expression pattern.[24,37] Consequently, dual-lock- or single-enzyme-activatable probes (*e.g.*, GGT- or β-gal-specific probes) alone may not accurately detect all ovarian cancer when targeting cancer subtypes with insufficient expression of their respective enzymes, potentially leading to the false-negative results.[20,38] The occurrence of false-negative signals can lead to a delay in the optimal treatment window, exacerbate disease progression, and even worsen the spread of some

[a]*State Key Laboratory of Fine Chemicals, Frontier Science Center for Smart Materials, Dalian University of Technology, Dalian, 116023, China. E-mail: yangmw66@126.com; fanjl@dlut.edu.cn*

[b]*Liaoning Binhai Laboratory, Dalian, 116023, China*

infectious diseases.[39,40] Although the combined application of two single-enzyme probes could theoretically broaden biomarker detection, divergent physicochemical properties (*e.g.*, photobleaching rates, solubility, *etc.*) and pharmacokinetics profiles may compromise imaging consistency and capacity.[38,41] Thus, there is an urgent need for a unimolecular fluorescent probe capable of concurrently targeting both GGT and β-gal to mitigate false-negative signals in ovarian cancer diagnosis. To date, however, no such probe has been reported.

Herein, we present a novel unimolecular enzyme-activated near-infrared (NIR) fluorescent probe, **Cy-GGT–β-gal**, for effectively minimizing false-negative signals in ovarian cancer diagnosis through visualizing either GGT or β-gal (Scheme 1). In the skeleton of the designed platform, both GGT and β-gal-recognized groups are incorporated as initiators of fluorescence within a logical single benzene ring scaffold, which serve as a fluorescence quencher linked to a hemicyanine fluorophore *via* carbonate bonds. **Cy-GGT–β-gal** is initially non-fluorescence due to intramolecular charge transfer (ICT) inhibition by the caged electron-donating hydroxyl group. Fluorescence is restored only upon enzymatic cleavage by either GGT or β-gal, triggering intramolecular 1,4- or 1,6-elimination, respectively, to release the NIR-emitting fluorophore. In contrast to the single-enzyme probes (*e.g.*, **Cy-GGT** and **Cy-β-gal**), which fail to detect ovarian cancer cell lines with low target-enzyme expression, **Cy-GGT–β-gal** generates robust fluorescent signal across diverse ovarian cancer cell lines (SHIN3, OVCAR3, OVCAR5, A2780, SKOV3), effectively distinguishing cancer from normal cells (SNR > 6.1) and minimizing false-negative phenomenon. *In vivo* studies further demonstrate its utility for detecting tumor edges *via in situ* spraying, facilitating fluorescence-mediated tumor surgery, and monitoring of tumor lung metastases and nodular tissues with high SNR (~11.2). By targeting either enzymatic pathway, **Cy-GGT–β-gal** alleviates the diagnostic pitfall of false-negative results caused by tumor microenvironment heterogeneity, offering significant potential for clinical translation.

Results and discussion

Design and synthesis of Cy-GGT–β-gal

The heterogeneity of biomarker expression across ovarian cancer subtypes poses a significant challenge in diagnostic accuracy, particularly due to the risk of false-negative results that delay treatment and worsen patient outcomes. For instance, while GGT is highly overexpressed in SHIN3, OVCAR4, and OVCAR5 cell lines, its expression is minimal in SKOV3 and OVCAR3. Conversely, β-gal shows high activity in SHIN3 and OVCAR3 but limited presence in other cell lines. This variability complicates diagnostics, as single-enzyme-targeting probes may fail to detect certain subtypes, leading to unreliable results (Scheme 1A). Although combining two separate fluorescent probes can partially mitigate false negatives, discrepancies in their physicochemical properties and metabolic behaviors may compromise accuracy. To overcome this critical limitation, we developed **Cy-GGT–β-gal**, a unimolecular fluorescent probe engineered with dual enzyme-responsive capabilities (Scheme 1B). The molecular design integrates three components: (1) a hemicyanine fluorophore (**Cy-OH**) that provides excellent NIR emission for fluorescent imaging; (2) a dual-enzyme recognition system incorporating both GGT and β-gal substrate moieties positioned on a single benzene ring scaffold; and (3) carbonate linkages that serve as cleavable connections between the fluorophore and the recognition units. The fluorescence of **Cy-GGT–β-gal** is in the "off" state due to the effective inhibition of its ICT process. Upon encountering either GGT or β-gal, the respective enzyme recognition moiety undergoes cleavage, triggering an elimination cascade that ultimately releases the fluorescent reporter molecule (**Cy-OH**). This design ensures that regardless of which enzyme is overexpressed in a particular ovarian cancer subtype, the probe can generate a consistent fluorescence signal, thereby enhance detection sensitivity and minimizing false-negative results (Scheme 1C).

The synthesis of **Cy-GGT–β-gal** began with the preparation of the hemicyanine fluorophore (**Cy-OH**) as the signaling component (Scheme S1). Concurrently, we synthesized the dual-enzyme responsive scaffold from 2,4-dihydroxysalicylaldehyde through a carefully optimized multi-step sequence. The integration of these components was achieved through carbonate bond formation using triphosgene chemistry. For precisely evaluating the performance advantages of our designed fluorescent probe, we synthesized two comparable single-enzyme responsive agents, **Cy-GGT** and **Cy-β-gal**, through similar synthetic methods and recognition mechanisms (Fig. 1C and Scheme S2). All intermediates and final compounds were rigorously characterized by ^{1}H NMR, ^{13}C NMR, and HR-MS to confirm their structural integrity and purity (SI).

Investigation of photophysical properties in solution

After obtaining **Cy-GGT–β-gal**, the response characteristics of the probe toward GGT or β-gal were systematically investigated. The absorption spectrum of **Cy-GGT–β-gal** exhibits prominent absorption peak centered at 600 nm (Fig. S1) with negligible fluorescence emission (Fig. 1A), confirming effective fluorescence quenching in its native state. Upon exposure to GGT, the absorption peak at 600 nm diminished while a new band emerged at 670 nm (Fig. S1), accompanied by progressive enhancement of fluorescence emission at 720 nm (Fig. 1A). This fluorescence change reached maximum intensity after 40 minutes (Fig. S3) and displayed excellent correlation with GGT concentrations (Fig. S4), demonstrating the probe's quantitative detection capabilities. Remarkably, when challenged with β-gal instead of GGT, **Cy-GGT–β-gal** exhibited similar spectroscopic changes (Fig. S2 and 1B), with comparable fluorescence kinetics (35 minutes to maximum intensity, Fig. S3) and similar concentration-dependence (Fig. S5). This dual-responsive behavior represents a significant advancement over conventional single-enzyme probes, as it enables detection regardless of which enzyme is overexpressed in various ovarian cancer subtypes. To fully appreciate the innovative aspects of our unimolecular design, we conducted comparative spectroscopic analyses with the single-enzyme probes **Cy-GGT** and **Cy-β-gal**. Unlike **Cy-GGT–β-gal**, these conventional probes exhibited

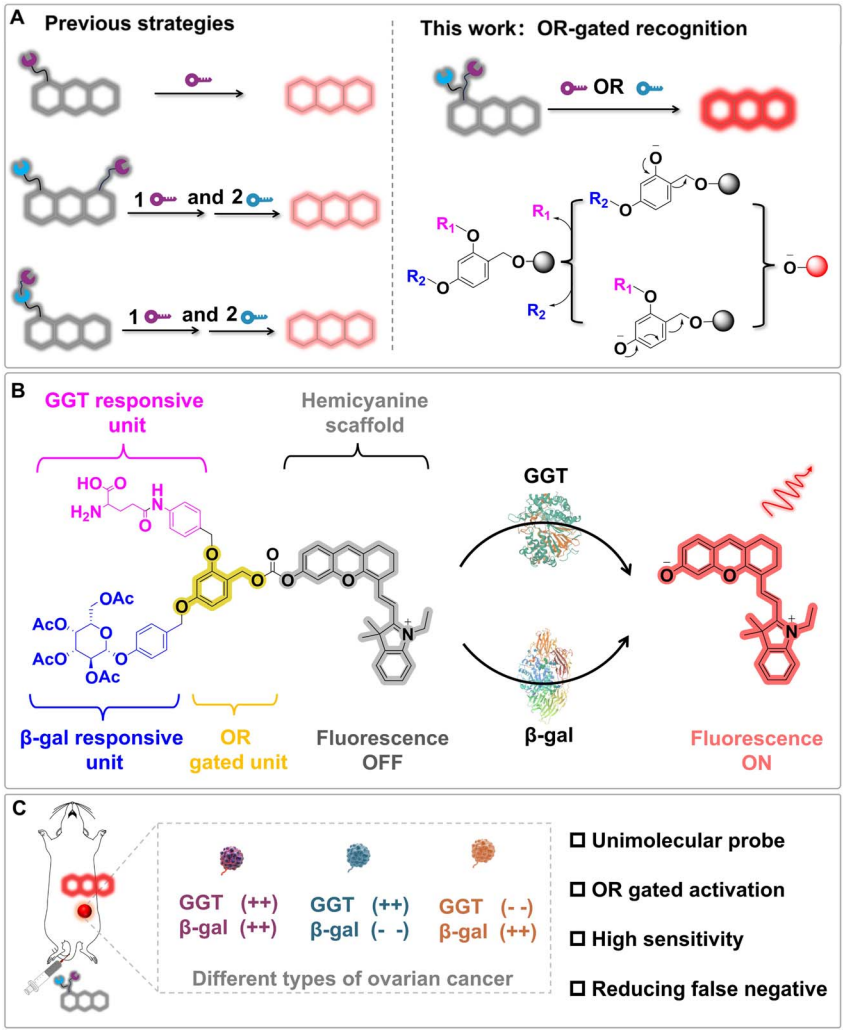

Scheme 1 Schematic diagram of OR gated probe in cancer detection. (A) Comparison of previous strategies and this work. (B) The structure and response mechanism of the **Cy-GGT–β-gal** probe. (C) Illustration of the application of probe in minimizing false negative.

strictly mono-responsive behavior. **Cy-GGT** generated fluorescence signals exclusively in the presence of GGT, showing no response to β-gal even at high concentrations (Fig. 1C and S9). Conversely, **Cy-β-gal** activated only with β-gal exposure while remaining completely silent to GGT (Fig. 1C and S10). The selectivity of **Cy-GGT–β-gal** was then validated by challenging various biologically stimulants such as NADH, NTR, APN, ALP, BSA, GSH, H_2O_2, Hcy and Cys. As shown in Fig. 1D, under the excitation of 660 nm, only GGT and β-gal can induce a remarkable fluorescence enhancement of probe at 720 nm, whereas other analytes cause negligible changes in fluorescence intensity even after a 120 min incubation period. These results demonstrated the excellent selectively of **Cy-GGT–β-gal**. We have conducted additional selectivity experiments testing **Cy-GGT–β-gal** against various hydrolytic enzymes under identical conditions (5 μM probe, PBS pH 7.4, 37 °C, 2 h): acetylcholinesterase (AChE, 10 U mL^{-1}), butyrylcholinesterase (BChE), chymotrypsin, carboxylesterase 1 (CE1), carboxylesterase 2 (CE2), and monoacylglycerol lipase (MAGL) (Fig. S8). All six enzymes have shown negligible fluorescence enhancement, while GGT and β-gal have generated robust responses. These results have confirmed that probe activation requires specific enzymatic cleavage by GGT or β-gal rather than non-specific hydrolysis by common esterases, proteases, or lipases.

The underlying mechanism responsible for the dual-activation capability of **Cy-GGT–β-gal** was elucidated through detailed structural and kinetic analyses. As illustrated in Fig. 1E, GGT triggers a 1,6-elimination pathway while β-gal initiates a 1,4-elimination cascade, both culminating in the release of identical **CyI-OH** fluorophores. This mechanistic convergence represents a key innovation in our molecular design: regardless of which enzymatic pathway is activated, the same reporter molecule is generated, ensuring consistent signal output across diverse tumor environments. To validate our findings, we conducted an ESI-MS analysis of the reaction products. As illustrated in Fig. S6 (SI), the reaction mixture of probe **Cy-GGT–β-gal** with GGT revealed two distinct mass peaks at $m/z = 398.2102$ and 577.1812, which corresponded precisely to the calculated molecular masses of the expected compounds **CyI-OH** ($[M]^+ = 398.2099$) and **P1** ($[M + H]^+ = 577.1916$). Similarly, Fig. S7

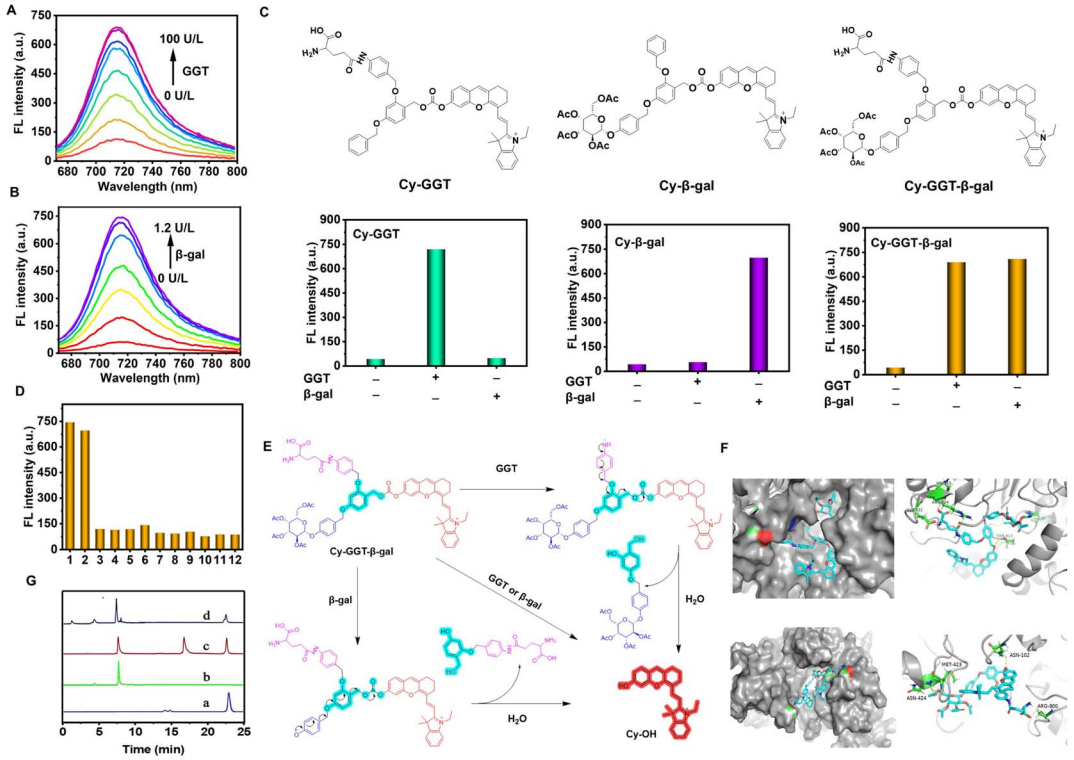

Fig. 1 The fluorescence spectrum changes of **Cy-GGT–β-gal** (5 μm) in PBS buffer (10.0 mm, pH 7.4, containing 20% DMSO), after introduction of (A) GGT (0.0–100.0 U L^{-1}) and (B) β-gal (0.0–1.2 U L^{-1}). (C) The chemical structure of probes **Cy-GGT**, **Cy-β-gal** and **Cy-GGT–β-gal** and the fluorescence intensity of **Cy-GGT**, **Cy-β-gal** and **Cy-GGT–β-gal** (5 μM in PBS, pH = 7.4, 20% DMSO) at 2 h under different stimuli (GGT, 100 U L^{-1}; β-gal, 1.2 U L^{-1}). The above assays were performed at 37 °C without further modification. (D) The fluorescence intensity of **Cy-GGT–β-gal** (5 μm) at 720 nm in various biological species (1, GGT; 2, β-gal; 3, NADH; 4, NTR; 5, APN; 6, ALP; 7, BSA; 8, GSH; 9, H_2O_2; 10, Hcy; 11, Cys; 12, PBS). (E) Proposed mechanism for the reaction between **Cy-GGT–β-gal** and GGT or **Cy-GGT–β-gal** and β-gal. (F) Molecular docking analysis of **Cy-GGT–β-gal** interactions: stereoscopic images showing **Cy-GGT–β-gal** (blue) docked with GGT (grey, upper left) and β-gal (grey, lower left) using the flexible docking module in Discovery Studio, with corresponding LigPlot schematic diagrams illustrating the secondary structure interactions (upper and lower right, respectively). (G) HPLC chromatographic analysis was performed on several samples: pure **Cy-GGT–β-gal** (a), **CyI-OH** (b), a mixture of **Cy-GGT–β-gal** with GGT (c) and a mixture of **Cy-GGT–β-gal** with β-gal. Detection was carried out at 670 nm for lanes (a–d). The reaction mixture, consisting of ACN/water (60 : 40) and $NaHCO_3$ (5 equiv.), was analyzed after a 2-hour incubation period.

demonstrates that the reaction mixture of probe **Cy-GGT–β-gal** with β-gal exhibited two characteristic mass peaks at m/z = 398.2102 and 375.1501, which aligned excellently with the theoretical molecular weights of the anticipated compounds **CyI-OH** and **P2** ($[M + H]^+$ = 375.1551). These spectroscopic results provide strong confirmation of the proposed reaction mechanism and product formation. To further corroborate our findings, we employed High-Performance Liquid Chromatography (HPLC) analysis. The resulting chromatogram provided additional evidence for the simultaneous release of **CyI-OH** (Fig. 1G). After a 2 hours reaction period with GGT or β-gal, the peak corresponding to the probe **Cy-GGT–β-gal** (retention time 22 min) was almost entirely absent. Concurrently, two new peaks emerged at retention times of 8 min, which aligned precisely with the retention times of pure **CyI-OH**.

To comprehend the possible interaction and cutting mechanisms, molecular docking was performed. **Cy-GGT–β-gal** was separately docked with GGT and β-gal using flexible docking module in Discovery Studio. The docking analyses revealed that the molecular backbone of **Cy-GGT–β-gal** fits remarkably well into the catalytic pocket of GGT, exhibiting a strong binding affinity (−9.9 kcal mol^{-1}) (Fig. 1F). This favorable interaction is stabilized by multiple hydrogen bonds with specific amino acid residues, including HIS 87 (O–H), THR 413 (O–H), HIS 514 (O–H), GLU 522 (H–O), and ARG 524 (O–H), as shown in Fig. 1F. Similarly, when docked with β-gal, **Cy-GGT–β-gal** effectively nestles within the protein cavity, forming critical hydrogen bond interactions with residues ASN-102 (O–H), MET-423 (O–H), ASN-424 (O–H), and ARG-800 (O–H), resulting in a significant binding energy of −8.6 kcal mol^{-1} (Fig. 1F). These molecular modeling results provide structural insights into the dual-enzyme recognition capabilities of the designed probe.

In vitro distinguishing and fluorescent imaging of cancer cells

Encouraged by the promising results obtained in solution, we further investigated the potential of **Cy-GGT–β-gal** and comparable molecules, **Cy-GGT** and **Cy-β-gal**, for visualizing GGT or β-gal activity in cellular environments. In this section, several ovarian cancer cell lines (SHIN3, SKOV3, OVCAR3, OVCAR5, and A2780) as well as normal ovarian epithelial cells (IOSE80) were selected as experimental samples. We first characterized

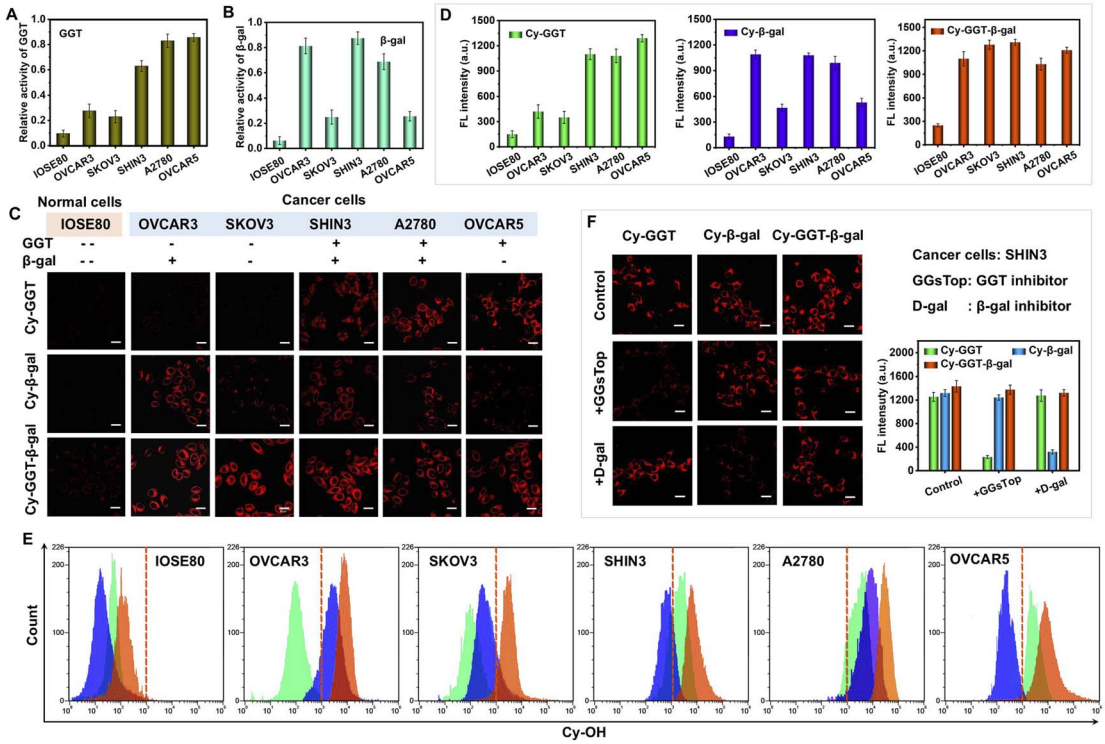

Fig. 2 (A) β-Galactosidase and (B) γ-GGT relative activity per protein abundance in lysate of IOSE80, OVCAR3, SKOV3, SHIN3, A2780 and OVCAR5 cells. Data represent mean ± SD from a single experiment in triplicate. (C) Comparison of **Cy-GGT**, **Cy-β-gal** and **Cy-GGT–β-gal** on the fluorescence imaging of live cells. **Cy-GGT**, **Cy-β-gal** and **Cy-GGT–β-gal** (5 μM) was incubated with OVCAR3, SKOV3, SHIN3, A2780, OVCAR5 and IOSE80 cells at 37 °C for 1 h (λ_{ex}: 640 nm and λ_{em}: 670–750 nm). In normal cells, ultralow enzymes expression is denoted by "––"; in cancer cells, low expression is indicated by "–", and high expression is marked by "+". Scale bars: 10 μm. (D) Fluorescence emission intensities of red channel were measured as averages of 5 regions of interest (ROIs) from different probe in IOSE80, OVCAR3, SKOV3, SHIN3, A2780 and OVCAR5 cells. Error bar = RSD ($n = 5$). (E) Flow cytometry analysis of **Cy-GGT** (green), **Cy-β-gal** (blue) and **Cy-GGT–β-gal** (red) in living IOSE80, OVCAR3, SKOV3, SHIN3, A2780 and OVCAR5 cells. (F) Comparison of **Cy-GGT**, **Cy-β-gal** and **Cy-GGT–β-gal** on the fluorescence imaging of SHIN3 cells. **Cy-GGT**, **Cy-β-gal** and **Cy-GGT–β-gal** (5 μM) was incubated with SHIN3 cells at 37 °C for 1 h or pretreated cells with GGsTop (0.5 mM, GGT inhibitor) or D-gal (0.5 mM, β-gal inhibitor) for 1 h before incubation with probe (λ_{ex}: 640 nm and λ_{em}: 700–750 nm). Scale bars: 10 μm.

the differential enzyme expression profiles across various ovarian cancer subtypes. As shown in Fig. 2A and B, GGT and β-gal displayed strikingly heterogeneous distribution patterns. SHIN3, OVCAR5, and A2780 cells exhibited high (+) GGT activity, whereas SKOV3 and OVCAR3 showed low (–) GGT expression. Conversely, β-gal was highly expressed in SHIN3, OVCAR3, and A2780 cells but remained low in SKOV3 and OVCAR5. Normal IOSE80 cells demonstrated minimal expression (––) of both enzymes. The heterogeneous expression of this enzyme introduces significant uncertainty into the early diagnosis of cancer. Before proceeding with cellular imaging, the cytotoxicity of **Cy-GGT–β-gal** was evaluated using MTT assays. As shown in Fig. S11–S16, all six cell lines demonstrated negligible cytotoxicity even at concentrations significantly higher than those required for imaging. This excellent biocompatibility profile established a solid foundation for subsequent cellular and *in vivo* studies.

To quantitatively demonstrate the superiority of our dual-responsive design, we performed parallel imaging experiments using single-enzyme probes **Cy-GGT** and **Cy-β-gal**. As shown in Fig. 2C and D, **Cy-GGT** generated strong signals only in GGT-overexpressing cells (SHIN3, A2780, OVCAR5) but failed to detect OVCAR3 and SKOV3 cells despite their malignant nature. Similarly, **Cy-β-gal** effectively visualized β-gal-rich cells (OVCAR3, SHIN3, A2780) but missed SKOV3 and OVCAR5 cancer cell. Excitingly, after treatment with **Cy-GGT–β-gal**, all five ovarian cancer cell lines (SHIN3, SKOV3, OVCAR3, OVCAR5, and A2780) exhibited significant NIR fluorescent signals (Fig. 2C), which correlates with the overexpression of GGT or β-gal in malignant tumor cells. In stark contrast, normal IOSE80 cells displayed no detectable fluorescent signal, demonstrating the excellent specificity of the probe for malignant cells. In addition, flow cytometry analysis across all cell lines provided compelling quantitative evidence of **Cy-GGT–β-gal**'s superior performance (Fig. 2E). The subcellular localization experiments were performed in living SHIN3 cells and confirmed that **Cy-OH** is mainly distributed in mitochondria (correlation coefficient of 0.89) after being activated (Fig. S17).

Then, we further validated the dual-activation mechanism through selective enzyme inhibition studies in SHIN3 cells, which express both target enzymes. Pretreatment with GGsTop (0.5 mM, a specific GGT inhibitor) completely suppressed **Cy-GGT** fluorescence activation, whereas D-gal (0.5 mM, a β-gal inhibitor) similarly blocked **Cy-β-gal** activation (Fig. 2F). In

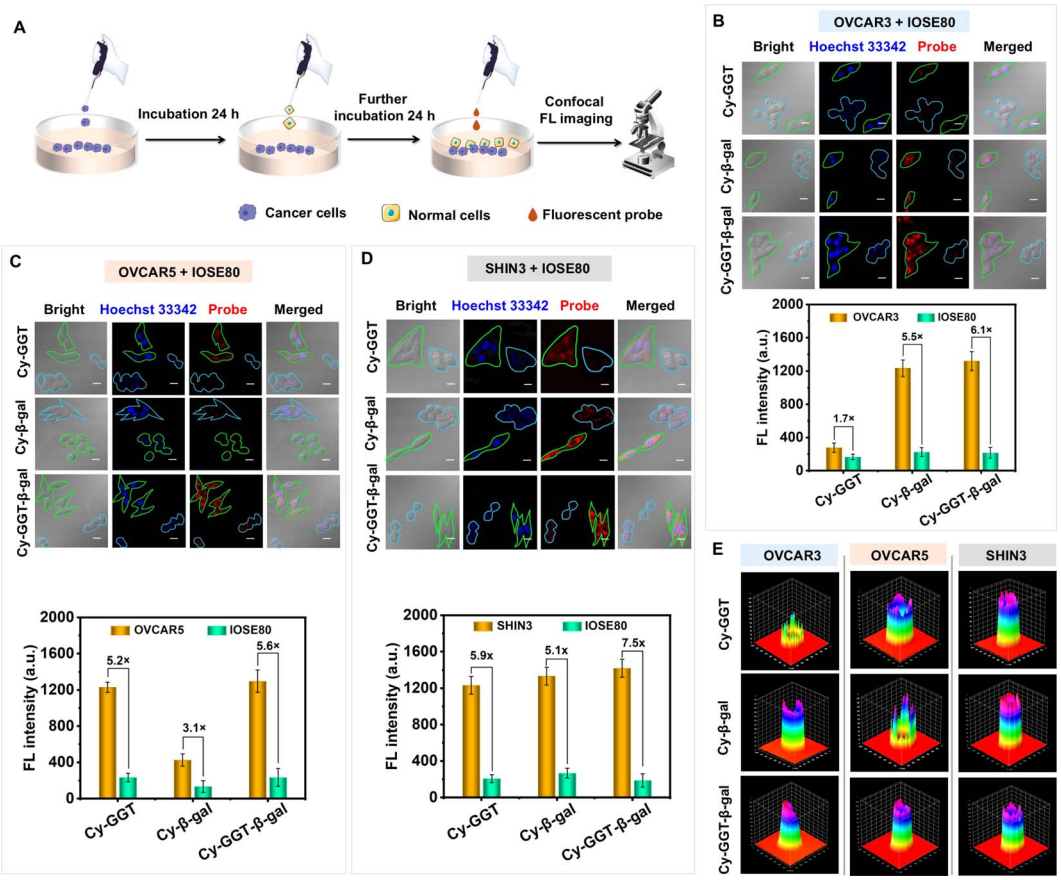

Fig. 3 (A) Fluorescence imaging diagram of probe treated mixed culture cells. Confocal fluorescence imaging of mixed cultures containing ovarian cancer cell (green area) lines OVCAR3 (B), OVCAR5 (C) or SHIN3 (D) with normal ovarian surface epithelial cells IOSE80 (blue area) after 1 hour treatment with probes **Cy-GGT**, **Cy-β-gal**, and **Cy-GGT–β-gal** (5 μM), with quantitative analysis of average fluorescence intensity differences between malignant and normal cells. Red channel: λ_{ex} = 640 nm, λ_{em} = 700–750 nm, blue channel: λ_{ex} = 405 nm, λ_{em} = 440–480 nm; scale bar = 20 μm. (E) 3D surface plots of the fluorescence intensity of the spheroids on the *z*-axis.

contrast, **Cy-GGT–β-gal** maintained strong fluorescence emission regardless of which inhibitor was applied, demonstrating remarkable resilience to single-enzyme inhibition. As long as one target enzyme remains active, efficient activation and release of visual signals for cancer diagnosis can be achieved. Collectively, these experimental results comprehensively validate that our probe has a significant advantage in minimizing false-negative during the detection of various types of ovarian cancer cells.

In clinical settings, identifying cancer cells solely from isolated cell cultures presents limitations for early tumor detection, as early-stage tumors typically consist of a heterogeneous mixture of normal and cancer cells.[42] To evaluate the practical applicability of **Cy-GGT–β-gal** under more challenging conditions, we conducted co-culture experiments with multiple cell lines. We strategically selected four cell lines with varying enzyme expression profiles to create three co-culture models: OVCAR3 (high β-gal, low GGT cancer cells)/IOSE80, OVCAR5 (high GGT, low β-gal cancer cells)/IOSE80, and SHIN3 (high expression of both enzymes)/IOSE80. The operation procedure of the cell co-culture models are shown in the Fig. 3A. Each co-culture system was then treated with **Cy-GGT**, **Cy-β-gal**, or **Cy-GGT–β-gal** for comparative imaging analysis. As shown in Fig. 3B–D, the co-culture systems enable clear differentiation between cancer cells (green regions) and normal cells (cyan areas) through distinct morphology and nuclear fluorescence labeling. In the OVCAR3/IOSE80 system (Fig. 3B), cells in the green region (OVCAR3 cells) exposed to either **Cy-β-gal** or **Cy-GGT–β-gal** demonstrated pronounced fluorescence signals with high SNR of 5.5 and 6.1, respectively. In contrast, cells treated with **Cy-GGT** exhibited minimal fluorescence enhancement, yielding a substantially lower SNR of 1.7. This differential response can be attributed to the overexpression of β-gal and the low expression of GGT in OVCAR3 cells. Conversely, in the OVCAR5/IOSE80 system (Fig. 3C), cancer cells demonstrated significant fluorescence upon **Cy-GGT** or **Cy-GGT–β-gal** treatment with high SNR, whereas **Cy-β-gal** induced minimal enhancement. In the SHIN3/IOSE80 system (Fig. 3D), all three probes generated enhanced fluorescence intensity and elevated SNR following treatment, consistent with SHIN3's characteristic high expression of both GGT and β-gal. These results further indicate that **Cy-GGT–β-gal** can be effectively activated in cell lines overexpressing either GGT or β-gal.

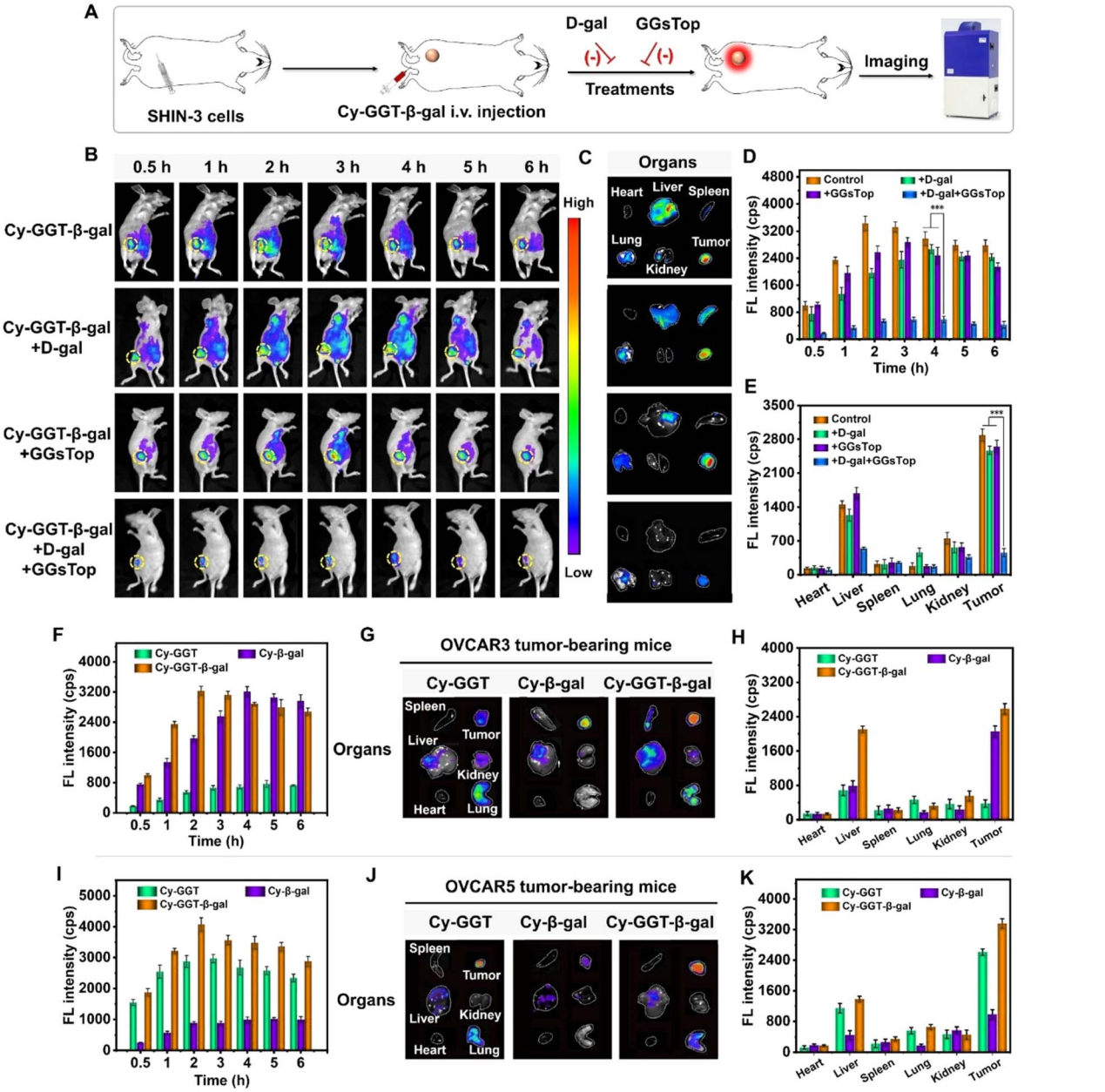

Fig. 4 (A) Establishment of xenotransplantation mouse model and real-time *in vivo* tumor imaging diagram. (B) *In vivo* fluorescence imaging of tumor-bearing mice after different treatments. GGsTop (0.5 mM, 50 μL) (a GGT inhibitor) or D-gal (0.5 mM, 50 μL) (a β-gal inhibitor) was used to inhibit the expression of GGT or β-gal in tumors. (C) Fluorescence images of tumor and main organs at 24 h after i.v. injection of **Cy-GGT–β-gal**. (D) Time-dependent fluorescence photographs for mouse receiving i.v. injection of **Cy-GGT–β-gal** (100 μM, 100 μL). (E) Fluorescence imaging of major organs and tumors at 24 h after injection. (F–H) Fluorescence imaging and fluorescent intensity tumor and main organs at 24 h after i.v. injection of **Cy-GGT** or **Cy-β-gal** or **Cy-GGT–β-gal** in OVCAR3 tumor-bearing mice. (I–K) Fluorescence imaging and fluorescent intensity tumor and main organs at 24 h after i.v. injection of **Cy-GGT** or **Cy-β-gal** or **Cy-GGT–β-gal** in OVCAR5 tumor-bearing mice (*t* tests, $n = 5$, mean ± SD, $^{*}p < 0.05$, $^{**}p < 0.01$, $^{***}p < 0.001$, $^{****}p < 0.0001$).

To further bridge the gap between cellular studies and *in vivo* applications, we developed three-dimensional (3D) multicellular spheroid (MCS) models derived from OVCAR3, SHIN3, and OVCAR5 cells. These spheroids more faithfully recapitulate the solid tumor architecture, including diffusion gradients and cell–cell interactions. As shown in Fig. S18–S20, treatment of MCSs with **Cy-GGT–β-gal** resulted in significantly enhanced fluorescence across all three cell lines, confirming its dual-enzyme responsive activation in 3D MCS models. In contrast, MCSs treated with **Cy-GGT** displayed strong fluorescence only in OVCAR5 and SHIN3. Similarly, following **Cy-β-gal** treatment, only OVCAR3 and SHIN3 MCSs demonstrated robust fluorescence. These finding align with our previous cellular imaging results, further underscoring the superior ability of **Cy-GGT–β-gal** to overcome false-negative outcomes through its dual-activation mechanism. Moreover, confocal Z-stack imaging

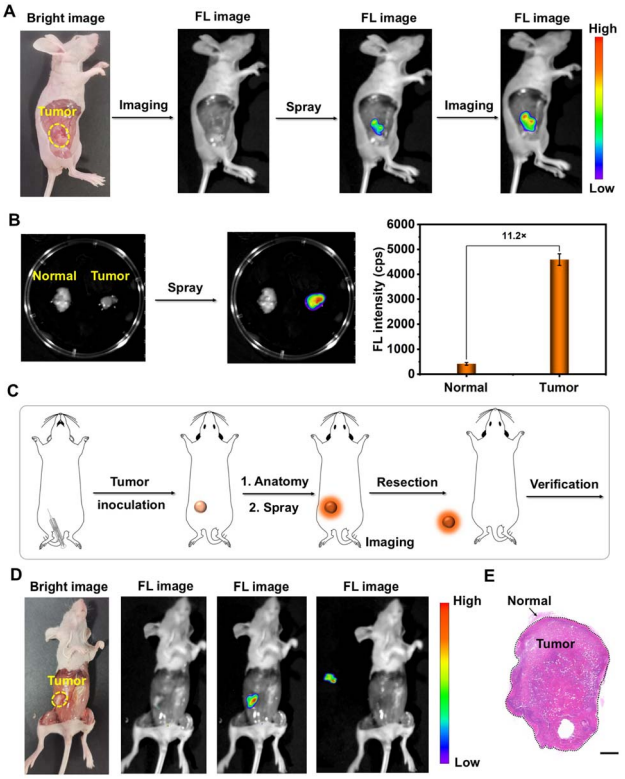

Fig. 5 Imaging image-guided resection by spraying **Cy-GGT–β-gal** in bare BABL/c mice bearing SHIN3 xenograft tumor. (A) *In situ* spraying imaging *in vivo*. (B) *In vitro* imaging of tumor tissue and normal tissue through spraying probe **Cy-GGT–β-gal** for 30 min and statistical fluorescence intensities. (C) Diagram of image-guided excision of spray probe **Cy-GGT–β-gal**. (D) Image-guided resection by spraying probe **Cy-GGT–β-gal**. (E) H&E staining of the resected tumors.

revealed that **Cy-GGT–β-gal** penetrates deeply throughout the spheroid depth (Fig. 3E), with uniform signal distribution from surface to core. This penetration capability is essential for accurate diagnosis and surgical guidance of deep-seated tumor tissues. These observations in increasingly complex biological models provide compelling evidence that **Cy-GGT–β-gal** not only responds effectively to either GGT or β-gal enzymatic activity but also achieves substantial tissue penetration and consistent detection across heterogeneous tumor environments.

In vivo fluorescence imaging of xenograft tumor models

Subsequently, tumor xenograft models were established by inoculating SHIN3, OVCAR3, and OVCAR5 cells into nude BALB/c mice to investigate the *in vivo* diagnostic performance of **Cy-GGT–β-gal**. Under tumor development as depicted in Fig. 4A, mice were pre-anesthetized and selective enzyme inhibitors were administered prior to intravenous injection of **Cy-GGT–β-gal**. The activation and biodistribution of probe were then monitored using an *in vivo* imaging system, allowing for validation of its dual-activation mechanism under physiological conditions.

Following tail vein administration of **Cy-GGT–β-gal**, significant NIR fluorescence signals specifically localized to tumor sites within 4 hours post-injection, with remarkable signal retention persisting for at least 24 hours (Fig. 4B and D). This rapid and sustained tumor-specific activation demonstrates the probe's excellent target specificity in living systems. When tumors were pre-treated with either D-gal (β-gal inhibitor) or GGsTop (GGT inhibitor), **Cy-GGT–β-gal** maintained strong fluorescence activation patterns comparable to uninhibited controls. Most significantly, the fluorescence signal become negligible throughout the observation period only both enzymes are simultaneously inhibited (D-gal + GGsTop). This resilience to single-enzyme inhibition provides compelling *in vivo* evidence of the probe's dual-activation capability, ensuring detection and preventing false-negative outcomes. *Ex vivo* imaging at 24 hours post-injection revealed that activated **Cy-GGT–β-gal** remained predominantly localized within tumor tissues, with hepatic clearance serving as the primary metabolic pathway (Fig. 4C and E). This favorable biodistribution profile enhances tumor-specific detection while minimizing background interference from normal tissues.

To rigorously validate the ability of our unimolecular probe to minimize false-negative outcomes in heterogeneous tumor environments, we systematically evaluated **Cy-GGT–β-gal** alongside single-enzyme probes in mouse xenograft models derived from OVCAR3 and OVCAR5 ovarian cancer subtypes, which exhibit contrasting enzyme expression profiles. In OVCAR3 tumor-bearing mice, intravenous administration of **Cy-GGT–β-gal** (100 μM, 100 μL) generated pronounced NIR fluorescence in tumor region. The signal intensity peaked at approximately 8 hours post-injection and remained stable throughout the extended observation period (Fig. S21A and 4F). When parallel mice received the single-enzyme probe **Cy-GGT**, only minimal fluorescence was detected in the tumor region. This negligible response directly demonstrates the false-negative issue: the GGT-specific probe failed to detect these tumors due to their low GGT expression, despite their malignant nature. Conversely, administration of **Cy-β-gal** produced strong fluorescence comparable to that of **Cy-GGT–β-gal**, confirming the high β-gal activity in these tumors. In OVCAR5 xenograft models, a complementary pattern emerged. Following **Cy-GGT–β-gal** administration, robust tumor-specific fluorescence developed, reaching peak intensity around 12 hours post-injection (Fig. S21B and 4I). The **Cy-GGT** probe produced similarly strong signals in these tumors, reflecting their high GGT expression. However, **Cy-β-gal** resulted in minimal fluorescence enhancement, highlighting another potential false-negative scenario where β-gal-specific probes would fail to detect these GGT-dominant tumors. *Ex vivo* imaging of excised organs and tumors at 24 hours post-injection provided additional insights into probe biodistribution (Fig. 4G, H and J, K). Tumors treated with **Cy-GGT–β-gal** consistently exhibited the most intense fluorescence among all examined tissues, regardless of their specific enzyme expression profile. The liver showed the highest fluorescence intensity among normal organs, indicating hepatobiliary clearance as the primary excretion pathway. These

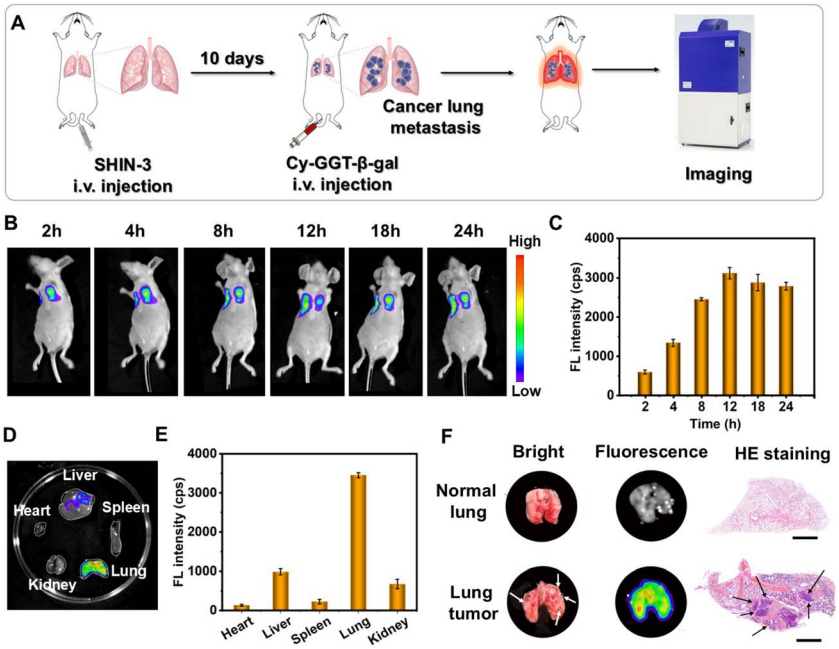

Fig. 6 *In vivo* lung metastasis imaging. (A) Schematic illustration of the lung metastasis model establishment timeline and real-time tumor imaging. (B) Time-dependent red fluorescence images of after intravenous injection of **Cy-GGT–β-gal**. (C) Mean fluorescence intensity of tumors analyzed. (D) Fluorescence imaging of major organs and tumors at 24 h after injection. (E) Mean fluorescence intensity quantification of Fig. 6D. (F) Photographs and H&E staining of the lung cancer metastasis and normal mouse lungs 24 hours after **Cy-GGT–β-gal** injection.

biodistribution patterns were consistent across experimental groups and aligned with the *in vivo* imaging results.

While single-enzyme probes inevitably failed to detect certain tumor subtypes due to insufficient target enzyme expression, **Cy-GGT–β-gal** consistently generated strong tumor-specific signals across diverse cancer models with varying enzyme profiles.[43] This universal detection capability represents a significant advancement in achieving more reliable cancer imaging, which has the potential to improve diagnostic accuracy.

Image-guided resection and visualization of cancer lung metastasis

Tumor fluorescence surgery navigation significantly enhances the accuracy and safety of tumor surgery through its triple advantages of "visualizing tumor boundaries + protecting normal tissues + optimizing treatment decisions", and it is an important part of modern precision medicine.[43,44] Encouraged by its excellent performance in diagnostic imaging, we further evaluated **Cy-GGT–β-gal** for its potential in image-guided tumor resection applications. Initially, we demonstrated that spraying **Cy-GGT–β-gal** directly onto the tissue could accurately highlight the tumor *in situ*, as shown in Fig. 5A. In contrast, prior to **Cy-GGT–β-gal** application, the same region exhibited negligible fluorescent signal. The probe's exceptional performance was also evident in *ex vivo* tissue differentiation, where freshly excised tumor and normal tissues were clearly distinguishable following *in situ* application of **Cy-GGT–β-gal**. Quantitative analysis revealed an impressive SNR of 11.2, which remained stable for at least 2 hours, thereby enabling precise identification of cancer tissues (Fig. 5B). Based on these promising results, we performed image-guided surgical resection (Fig. 5C). Following **Cy-GGT–β-gal** application, clearly defined fluorescent tissue was precisely excised using a scalpel (Fig. 5D). Subsequent probe application to the resection site yielded no detectable fluorescence signal, confirming complete tumor removal. Histopathological analysis *via* H&E staining validated these findings, demonstrating that the entire boundary of the resected tumor tissue was successfully differentiated from normal tissue with minimal residual negative margins (Fig. 5E). The straightforward spray application method further enhances the translational potential of **Cy-GGT–β-gal**, offering a practical approach for clinical implementation.

The detrimental effects of cancer metastasis go beyond localized organ destruction, involving systemic pathological alterations and substantially increasing treatment challenges.[45] Therefore, the early diagnosis of cancer metastasis is critical, as it provides real-time and dynamic biological information to facilitate the development of precision medicine. We established a BALB/c mouse cancer lung metastatic model carrying SHIN3 xenograft tumor. This model poses a significant diagnostic challenge compared to primary tumors, as metastatic nodules are typically smaller, more dispersed, and embedded within normal tissue. Ten days after intravenous injection of SHIN3 tumor cells (1×10^6), **Cy-GGT–β-gal** was administered *via* tail vein injection for imaging (Fig. 6A). As shown in Fig. 6B and C, the pulmonary fluorescence intensity progressively increased from 2 hours post-injection, reaching maximum intensity at approximately 12 hours. This kinetic profile

demonstrates the probe's efficient accumulation in metastatic lesions. After 24 hours, mice were euthanized for *ex vivo* imaging analysis, revealing pronounced NIR fluorescence signals specifically in lungs from tumor-bearing mice, while negligible fluorescence was observed in lungs from normal mice administered with the same condition (Fig. 6D and E). Macroscopic examination revealed distinct metastatic nodules throughout the lungs of SHIN3 tumor-bearing mice, whereas the lungs of normal mice exhibited healthy morphological characteristics without evidence of metastatic lesions (Fig. 6F). These macroscopic observations were subsequently confirmed by histopathological analysis using H&E staining of lung tissue specimens, which demonstrated clear evidence of tumor infiltration in the metastasis model.

The clinical translation of any imaging agent necessitates a thorough biocompatibility assessment. Our comprehensive evaluation of **Cy-GGT–β-gal** revealed an excellent safety profile. Healthy mice administrated the probe (100 μM, 100 μL) showed no significant differences in body weight compared to control groups (Fig. S22A). Hematological parameters, including red and white blood cell counts remained within normal ranges after administration (Fig. S22B and C), indicating no acute or chronic hematological toxicity. Liver and kidney function markers, including ALT, AST, ALB, BUN, and CRE, showed no significant abnormalities compared to control groups (Fig. S22D–H), demonstrating that **Cy-GGT–β-gal** does not induce hepatic or renal toxicity. Additionally, histopathological examination of major organs (heart, liver, spleen, lung, kidney) revealed no significant tissue damage or inflammatory changes (Fig. S22I), further confirming the probe's excellent biocompatibility.

These results demonstrate that **Cy-GGT–β-gal** can serve as a powerful fluorescent agent for precise tumor imaging and resection guidance. The ability to detect small metastatic nodules while maintaining excellent biocompatibility highlights the significant potential of this unimolecular dual-enzyme responsive probe for comprehensive cancer imaging applications, ranging from primary tumor visualization to metastasis detection.

Conclusions

In this study, we developed **Cy-GGT–β-gal**, an innovative unimolecular NIR fluorescent probe designed to minimizes the critical challenges of false-negative diagnoses in ovarian cancer by simultaneously targeting two key biomarkers: γ-glutamyl transpeptidase (GGT) and β-galactosidase (β-gal). The probe's dual-enzyme-responsive design enables selective NIR fluorescence activation through an intramolecular elimination mechanism upon interaction with either enzyme, ensuring broad detection coverage across heterogeneous tumor subtypes. Comprehensive investigations demonstrate that while conventional single-enzyme probes failed to detect cancer cells with low expression of their respective targets, **Cy-GGT–β-gal** achieves universal recognition of multiple ovarian cancer cell lines, distinguishing them from normal cells with high specificity (SNR > 6.1). *In vivo* studies revealed rapid tumor accumulation within 4 hours post-injection, with sustained signal retention for 24 hours, facilitating high-contrast visualization of primary tumors, metastatic lesions, and surgical margins (SNR ∼ 11.2). Furthermore, the image-guided surgical applications, simple spray application method, and excellent biocompatibility profile of probe further support its potential for clinical translation. By addressing the limitations of single-enzyme probes through its unimolecular, dual-activatable design, **Cy-GGT–β-gal** represents a significant advancement in precision diagnostics for ovarian cancer, offering a promising platform to mitigate false-negative result in diagnostics.

Ethical statement

All procedures involving animals adhered to the guidelines outlined in the Guide for the Care and Use of Laboratory Animals issued by the National Institutes of Health. The research protocol received approval from the Animal Ethics Committee at Dalian University of Technology (protocol number: 20220726).

Author contributions

J. H. and J. F. conceived and designed the experiments for this project. J. H. performed the synthetic work and carried out the characterization of the compounds. J. H., C. L. and K. L. contributed to the photophysical experiments. J. H. and M. Y. conducted data analysis and prepared the initial manuscript, with all other authors contributing to revisions. X. P. supervised the work. All authors discussed the results and provided feedback on the manuscript.

Conflicts of interest

The authors declare no competing financial interests.

Data availability

The data supporting this article have been included as part of the supplementary information (SI). Supplementary information is available. See DOI: https://doi.org/10.1039/d5sc07381b.

Acknowledgements

This work was financially supported by the National Natural Science Foundation of China (21925802, 22338005, 22308049), Liaoning Binhai Laboratory (LBLB-2023-03), the Fundamental Research Funds for the Central Universities (DUT22LAB601), Science and Technology Project of Liaoning Province (2022JH25/10100007).

Notes and references

1 R. Dood, N. D. Fleming, R. L. Coleman, S. N. Westin and A. Sood, *J. Clin. Oncol.*, 2017, **35**, e17066.
2 M. G. Perrone, O. Luisi, A. De Grassi, S. Ferorelli, G. Cormio and A. Scilimati, *Curr. Med. Chem.*, 2020, **27**, 5675.

3 K. E. Scarberry, E. B. Dickerson, Z. J. Zhang, B. B. Benigno and J. F. McDonald, *Nanomedicine*, 2010, **6**, 399.
4 U. A. Matulonis, A. K. Sood, L. Fallowfield, B. E. Howitt, J. Sehouli and B. Y. Karlan, *Nat. Rev. Dis. Primers*, 2016, **2**, 16061.
5 R. Solidoro, A. Centonze, M. Miciaccia, O. M. Baldelli, D. Armenise, S. Ferorelli, M. G. Perrone and A. Scilimati, *Med. Res. Rev.*, 2024, **44**, 1800.
6 K. R. Kozak, M. W. Amneus, S. M. Pusey, F. Su, M. N. Luong, S. A. Luong, S. T. Reddy and R. Farias-Eisner, *Proc. Natl. Acad. Sci. U. S. A.*, 2003, **100**, 12343.
7 X. Zhou, Y. Liu, Q. Liu, L. Yan, M. Xue, W. Yuan, M. Shi, W. Feng, C. Xu and F. Li, *Theranostics*, 2019, **9**, 4597.
8 F. Zalfa, M. G. Perrone, S. Ferorelli, L. Laera, C. L. Pierri, A. Tolomeo, V. Dimiccoli, G. Perrone, A. De Grassi and A. Scilimati, *Cancers*, 2022, **14**, 3764.
9 R. F. Ozols, B. N. Bundy, B. E. Greer, J. M. Fowler, D. Clarke-Pearson, R. A. Burger, R. S. Mannel, K. DeGeest, E. M. Hartenbach and R. Baergen, *J. Clin. Oncol.*, 2003, **21**, 3194.
10 N. Duru, N. R. Pawar, E. W. Martin, M. S. Buzza, G. D. Conway, R. G. Lapidus, S. Liu, J. Reader, G. G. Rao, D. M. Roque, S. H. Leppla and T. M. Antalis, *Proc. Natl. Acad. Sci. U. S. A.*, 2022, **119**, e2201423119.
11 A. L. Vahrmeijer, M. Hutteman, J. R. van der Vorst, C. J. van de Velde and J. V. Frangioni, *Nat. Rev. Clin. Oncol.*, 2013, **10**, 507.
12 X. Dang, L. Gu, J. Qi, S. Correa, G. Zhang, A. M. Belcher and P. T. Hammond, *Proc. Natl. Acad. Sci. U. S. A.*, 2016, **113**, 5179.
13 F. Wang, Y. Zhu, L. Zhou, L. Pan, Z. Cui, Q. Fei, S. Luo, D. Pan, Q. Huang, R. Wang, C. Zhao, H. Tian and C. Fan, *Angew. Chem., Int. Ed.*, 2015, **54**, 7349.
14 P. Wang, Y. Fan, L. Lu, L. Liu, L. Fan, M. Zhao, Y. Xie, C. Xu and F. Zhang, *Nat. Commun.*, 2018, **9**, 2898.
15 S. M. Usama, F. Inagaki, H. Kobayashi and M. J. Schnermann, *J. Am. Chem. Soc.*, 2021, **143**, 5674.
16 L. Wang, Y. Huang, J. Wang, Y. Jiang, B.-P. Jiang, H. Chen, H. Liang and X.-C. Shen, *J. Am. Chem. Soc.*, 2025, **147**, 6707.
17 M. Nakadate, R. Kojima, N. Seike, R. Tachibana, K. Fujita, R. Tsuchiya, M. Kamiya, A. Plückthun and Y. Urano, *J. Am. Chem. Soc.*, 2025, **147**, 30684.
18 F. Xu, H. Li, Q. Yao, H. Ge, J. Fan, W. Sun, J. Wang and X. Peng, *Chem. Sci.*, 2019, **10**, 10586.
19 H. Zhang, C. Shi, F. Han, L. Cai, H. Ma, S. Long, W. Sun, J. Du, J. Fan and X. J. Peng, *Chem. Sci.*, 2023, **302**, 122365.
20 J. Yuan, H. Yang, W. Huang, S. Liu, H. Zhang, X. Zhang and X. Peng, *Chem. Soc. Rev.*, 2025, **54**, 341.
21 C. Zhao, W. Sun, Y. Zhu, X. Huang, Y. Sun, H.-Y. Wang, Y. Pan and Y. Liu, *J. Med. Chem.*, 2024, **67**, 22322.
22 Z. Cheng, S. Benson, L. Mendive-Tapia, E. Nestoros, C. Lochenie, D. Seah, K. Y. Chang, Y. Feng and M. Vendrell, *Angew. Chem., Int. Ed.*, 2024, **63**, e202404587.
23 Y. Peng, R. Mo, M. Yang, H. Xie, F. Ma, Z. Ding, S. Wu, J. W. Y. Lam, J. Du, J. Zhang, Z. Zhao and B. Z. Tang, *ACS Nano*, 2024, **18**, 26140.
24 D. Asanuma, M. Sakabe, M. Kamiya, K. Yamamoto, J. Hiratake, M. Ogawa, N. Kosaka, P. L. Choyke, T. Nagano, H. Kobayashi and Y. Urano, *Nat. Commun.*, 2015, **6**, 6463.
25 B. Feng, F. Chu, A. Bi, X. Huang, Y. Fang, M. Liu, F. Chen, Y. Li and W. Zeng, *Biotechnol. Adv.*, 2023, **68**, 108244.
26 M. Zhang, Z. Liu, L. Qiu, W. Ma and Z. Yang, *J. Clin. Oncol.*, 2024, **42**, 127.
27 Z.-Y. Hu, X.-Y. Chen, Y.-S. Yang, S.-J. Wang, Z.-G. Hu and K. Wang, *Coord. Chem. Rev.*, 2024, **501**, 215562.
28 K. Gu, Y. Xu, H. Li, Z. Guo, S. Zhu, S. Zhu, P. Shi, T. D. James, H. Tian and W.-H. Zhu, *J. Am. Chem. Soc.*, 2016, **138**, 5334.
29 H. Wang, X. Zhang, P. Li, F. Huang, T. Xiu, H. Wang, W. Zhang, W. Zhang and B. Tang, *Angew. Chem., Int. Ed.*, 2024, **63**, e202315861.
30 L. Li, B. Zhang, Y. Wang, H. Han, K. Chen, M. Li, Q. Fan, H. Zhang and Q. Shen, *Adv. Funct. Mater.*, 2025, 2502250.
31 L. He, D.-Q. Lu, H. Liang, S. Xie, C. Luo, M. Hu, L. Xu, X. Zhang and W. Tan, *ACS Nano*, 2017, **11**, 4060.
32 J. Ren, X. Gao, B. Song, W. Zhang and J. Yuan, *Chem. Eng. J.*, 2025, **512**, 162680.
33 S. Tanaka, Y. Kitagawa, M. Kamiya, T. Shimizu, Y. Urano and N. Saito, *Neuro-Oncology*, 2021, **23**, vi225.
34 Y. Hu, J. Liu, M. Xu and K. Pu, *J. Am. Chem. Soc.*, 2025, **147**, 7148.
35 Y. Shen, W. Li, Z. Zhou, J. Xu, Y. Li, H. Li, X. Zheng, S. Liu, X.-B. Zhang and L. Yuan, *Angew. Chem., Int. Ed.*, 2024, **63**, e202406332.
36 X. Wang, S. S. Liew, J. Huang, Y. Hu, X. Wei and K. Pu, *J. Am. Chem. Soc.*, 2024, **146**, 22689.
37 Y. Urano, M. Sakabe, N. Kosaka, M. Ogawa, M. Mitsunaga, D. Asanuma, M. Kamiya, M. R. Young, T. Nagano, P. L. Choyke and H. Kobayashi, *Sci. Transl. Med.*, 2011, **3**, 110ra119.
38 H.-W. Liu, L. Chen, C. Xu, Z. Li, H. Zhang, X.-B. Zhang and W. Tan, *Chem. Soc. Rev.*, 2018, **47**, 7140.
39 H. Ye, Y. Liu, L. Zhan, Y. Liu and Z. Qin, *Theranostics*, 2020, **10**, 4359.
40 J. Wang, L. Zhao and B. Yan, *Sens. Actuators, B*, 2022, **355**, 131297.
41 L. Wu, J. Huang, K. Pu and T. D. James, *Nat. Rev. Chem.*, 2021, **5**, 406.
42 H. Li, Q. Yao, F. Xu, N. Xu, R. Duan, S. Long, J. Fan, J. Du, J. Wang and X. Peng, *Biomaterials*, 2018, **179**, 1.
43 Y. Chen, T. Xiong, J. Du, J. Fan and X. Peng, *CCS Chem.*, 2024, **7**, 740.
44 H. Li, Q. Yao, W. Sun, K. Shao, Y. Lu, J. Chung, D. Kim, J. Fan, S. Long, J. Du, Y. Li, J. Wang, J. Yoon and X. Peng, *J. Am. Chem. Soc.*, 2020, **142**, 6381.
45 X. Xia, R. Wang, Y. Hu, S. Long, W. Sun, J. Fan and X. Peng, *Angew. Chem., Int. Ed.*, 2025, **64**, e202507157.